Computer Methods and Programs in Biomedicine 155 (2018) 61–73

Contents lists available at ScienceDirect

Computer Methods and Programs in Biomedicine

journal homepage: www.elsevier.com/locate/cmpb

Detection of multipoint pulse waves and dynamic 3D pulse shape of the radial artery based on binocular vision theory

Dongmei Lin[a,b,c], Aihua Zhang[a,b,c,*], Jason Gu[a,d], Xiaolei Chen[a,b,c], Qi Wang[a,b,c], Liming Yang[a,e], Yongxin Chou[a,f], Gongcai Liu[a,b,c], Jingyang Wang[g]

[a] College of Electrical and Information Engineering, Lanzhou University of Technology, Lanzhou, China
[b] Key Laboratory of Gansu Advanced Control for Industrial Processes, Lanzhou University of Technology, Lanzhou, China
[c] National Experimental Teaching Center of Electrical and Control Engineering, Lanzhou University of Technology, Lanzhou, China
[d] Department of Electrical and Computer Engineering, Dalhousie University, Halifax, Canada
[e] School of Electrical and Photoelectronic Engineering, Changzhou Institute of Technology, Changzhou, China
[f] School of Electrical and Automatic Engineering, Changshu Institute of Technology, Changshu, China
[g] College of Computer and Communication, Lanzhou University of Technology, Lanzhou, China

ARTICLE INFO

Article history:
Received 12 April 2017
Revised 7 November 2017
Accepted 24 November 2017

Keywords:
Binocular pulse detection system
Multipoint pulse waves
Dynamic three-dimensional pulse shape
Feature point extraction
Stereo matching

ABSTRACT

Background and objective: Pulse signals contain a wealth of human physiological and pathological information. How to get full pulse information is especially challenging, and most of the traditional pulse sensors can only get the pulse wave of a single point. This study is aimed at developing a binocular pulse detection system and method to obtain multipoint pulse waves and dynamic three-dimensional pulse shape of the radial artery.

Methods: The proposed pulse detection approach is image-based and implemented by two steps. First, a new binocular pulse detection system is developed based on the principle of pulse feeling used in traditional Chinese medicine. Second, pulse detection is achieved based on theories and methods of binocular vision and digital image processing. In detail, the sequences of pulse images collected by the designed system as experimental data are sequentially processed by median filtering, block binarization and inversion, area filtering, centroids extraction of connected regions, to extract the pattern centroids as feature points. Then stereo matching is realized by a proposed algorithm based on *Gong*-shape scan detection. After multipoint spatial coordinate calculation, dynamic three-dimensional reconstruction of the thin film shape is completed by linear interpolation. And then the three-dimensional pulse shape is achieved by finding an appropriate reference time. Meanwhile, extraction of multipoint pulse waves of the radial artery is accomplished by using a suitable reference origin. The proposed method is analyzed from three aspects, which are pulse amplitude, pulse rate and pulse shape, and compared with other detection methods.

Results: Analysis of the results shows that the values of pulse amplitude and pulse rate are consistent with the characteristics of pulse wave of the radial artery, and pulse shape can correctly present the shape of pulse in space and its change trend in time. The comparison results with the other two previously proposed methods further verify the correctness of the presented method.

Conclusions: The designed binocular pulse detection system and proposed algorithm can effectively detect pulse information. This tactile visualization-based pulse detection method has important scientific significance and broad application prospects and will promote further development of objective pulse diagnosis.

1. Introduction

Pulse is one of the most important and reliable source of information to evaluate the physiological state of the human body. In traditional Chinese medicine (TCM), pulse diagnosis is an effective method of disease diagnosis. To achieve objective pulse diagnosis, many researchers are dedicated to the exploration and study

* Corresponding author at: Lanzhou University of Technology, No. 287 Langongping Road, Qilihe District, Lanzhou 730050, China.
E-mail address: zhangaihua@lut.cn (A. Zhang).

https://doi.org/10.1016/j.cmpb.2017.11.025
0169-2607/

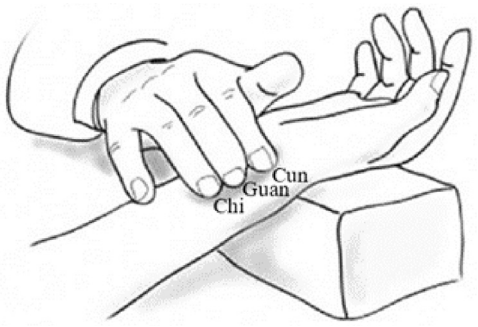

Fig. 1. Schematic diagram of pulse feeling in TCM.

of pulse sensor. The traditional pulse sensors are mainly piezoresistive, photoelectric and piezoelectric [1–4], which convert the spatial variation of pulse to a simple output of electrical signal that cannot reflect the detailed changes in the pulse of each point in the skin surface. Niu et al. used an ultrasonic probe to observe the movement of a vessel cross section [5,6]. Single-probe pulse sensor can only get limited information, which is quite different from pulse feeling used in TCM. As shown in Fig. 1, there are three important positions, Cun (寸), Guan (关) and Chi (尺), for pulse feeling in TCM, which are located at the wrist radial artery. Jin and coworkers studied the multipoint pulse sensor that can simultaneously measure pulses of Cun, Guan and Chi [7,8]. However, due to the sensor structure, size, performance, manufacturing processes and other factors, this method only measures a few points and cannot achieve simultaneous measurements in different parts of different vessel cross sections. In 2007, Jiang et al. applying laser triangulation measuring method detected skin surface vibration at the radial artery and achieved the pulse wave at a single point [9]. In 2013, Malinauskas et al. using laser triangulation method combined with projection moiré method measured the skin surface deformations of vascular graft under different input pressures [10]. The above optical measuring methods are constrained to be used only in laboratory and cannot be applied in practical situations, because of low signal-noise ratio, vulnerability to interference, and extreme harsh requirements for measurement environment. Zhang et al. designed and developed a bi-sensing pulse diagnosis instrument that could carry out simultaneous detection at Cun, Guan and Chi. This new method achieved good results [11–13]. Although the pulse sensor has been developed from the original single-position acquisition to three-position acquisition, from single-point acquisition to array-based multipoint acquisition, and greatly promoted the development of objective pulse diagnosis, there are some shortcomings, such as acquisition signal is limited, and the exact coincidence with actual pulse still needs to be further improved. Recently, Zhang et al. successfully developed a silk-molded flexible, ultrasensitive, and highly stable electronic skin for real-time monitoring of human physiological signals, such as pulse, heart rate and throat muscle group vibration, by attaching it to the human skin [14]. However, the pulse signal currently being measured using this electronic skin is single-channel.

To sum up, the existing usual rhythm detection methods and systems can only detect one dimensional electrical signals varying with time. Even the array pulse sensor can only detect a limited number of points on the same section. Moreover, the detected amplitude is not the longitudinal displacement caused by the pulse pulsation. Therefore, the three-dimensional (3D) shape of pulse cannot be reconstructed, and the concept of multi-dimensional pulse condition in TCM cannot be reflected. Furthermore, we cannot obtain accurate two-dimensional pulse information such as pulse width and pulse length, which are of great significance to reflect the physiological state of the human body.

If we can avoid or overcome the shortcomings in previous studies to a certain extent, and find a new method to fully detect the pulse information, to access dynamic 3D pulse shape, we could extract more pulse information and achieve a breakthrough in the field of objective pulse diagnosis. We have been devoted to the study of pulse tactile visualization method. A single-position dynamic pulse image acquisition system [15] was successfully developed, which could collect pulse images from one position of Cun, Guan and Chi. A three-position dynamic pulse image detection device [16] was also developed to synchronously collect pulse images of Cun, Guan and Chi. Consequently we achieved the image-based detection of pulse information. However, the 3D coordinates of spatial points are still defective based on monocular vision measurement principle, resulting in the accuracies of reconstructed 3D pulse shape and pulse wave not meeting the requirements of practical applications [17,18]. Binocular stereo vision imitates the way human and many animals catch spatial depth information using two eyes [19,20]. The use of binocular vision measurement technology for 3D detection is very suitable for our research. Therefore in this paper we describe a new binocular pulse detection system which was developed in order to access 3D pulse information, and which allows to analyze multipoint pulse waves over a rather big surface.

The remainder of this paper is organized as follows. In Section 2, binocular pulse detection system is introduced, and followed by the methods of pulse wave extraction and 3D reconstruction of pulse shape. Section 3 shows the experimental results and analysis, while Section 4 presents discussions of the method. The final conclusions are summarized in Section 5.

2. Methods

First, according to the principle of pulse feeling adopted in TCM and the pulse characteristics of human wrist radial artery, a binocular pulse detection system is developed. Second, multipoint pulse waves and dynamic 3D pulse shape are achieved by the proposed algorithm based on theories and methods of binocular vision and digital image processing.

2.1. Binocular pulse detection system

The system is introduced from four aspects, which are working principle, system hardware, system software and working process.

2.1.1. System working principle

The general working principle of the system is to visualize the pulsation of radial artery first, and then extract pulse information from visual information. The main part of the designed pulse detection system is shown in Fig. 2(a). A flexible thin film with mark patterns combined with an aluminum alloy cavity is used in the system to make an airbag probe which simulates the action of the finger pressing on radial artery. Pulse beating of the radial artery is reflected by the motion of the thin film. Two cameras above the probe synchronously collect dynamic images of thin film, i.e., the pulse images. Using the theories of imaging model and digital image processing, as well as binocular vision measurement principle, to process and analyze the pulse images, then the multipoint pulse amplitudes can be obtained. And multipoint pulse waves are acquired based on the collected pulse image sequences. 3D reconstruction of the thin film surface can be realized by the method of interpolation, then the 3D pulse shape is subsequently obtained by analyzing the motion and deformation of the thin film. Finally, dynamic 3D pulse shape is achieved. Fig. 2(b) shows a diagram of pulse detection.

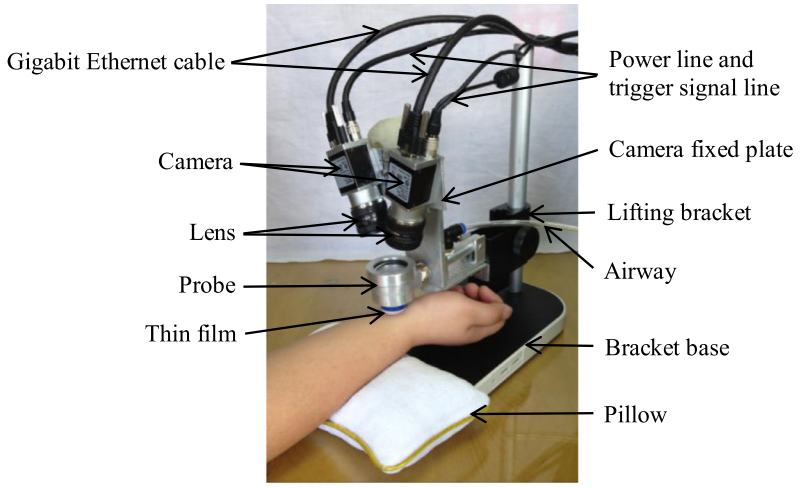

(a) Binocular pulse detection system (main part)

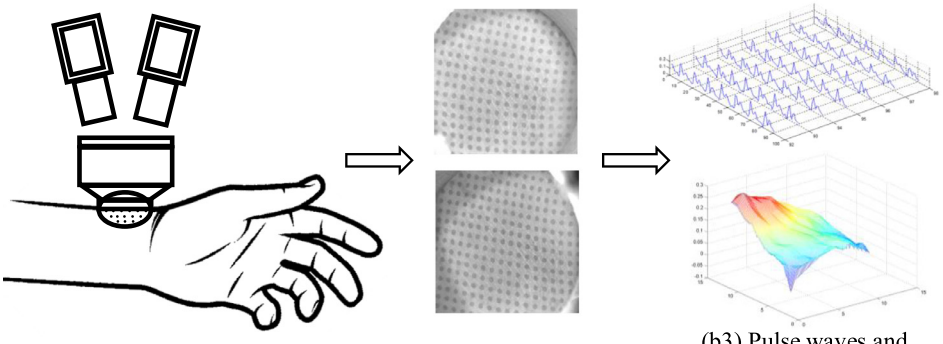

(b1) Pulse image collection (b2) Pulse images (b3) Pulse waves and 3D pulse shape

(b) Diagram of pulse detection

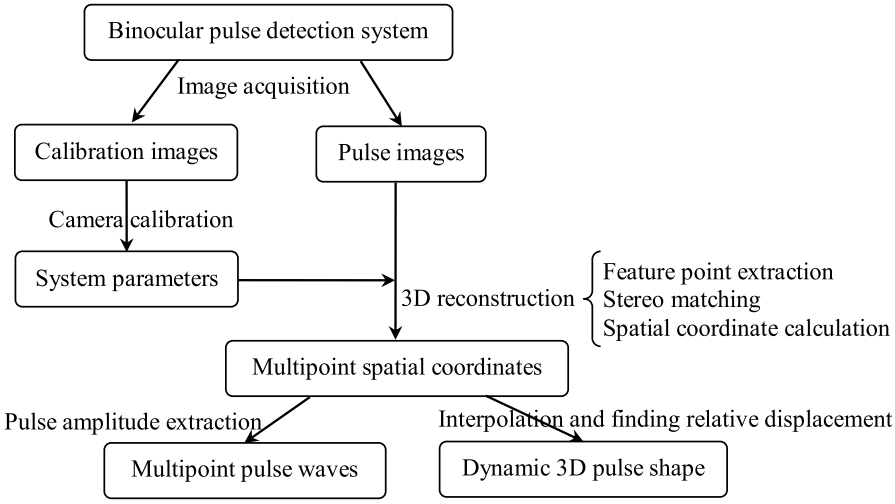

(c) The block diagram of pulse wave and 3D pulse shape detection

Fig. 2. Pulse detection.

2.1.2. System hardware

The hardware consists of an image acquisition module, a fixed module and an air supply module. Specifically, the image acquisition module used for collecting pulse images is composed of two industrial cameras, two industrial lenses, a probe (including an aluminum alloy cavity, a thin film printed with mark patterns, a transparent glass and a probe inner light source), two power lines, two trigger signal lines, a computer, two Gigabit Ethernet cables, a dual-port Gigabit Ethernet card (installed in the computer), a mp425 data acquisition module, a high precision calibration board and a backlight source. Fixed module adopts a lifting bracket, a bracket base, a camera fixed plate to fix the image acquisition device, and a little pillow for pulse feeling to fix the wrist of the subject. As pulse feeling in TCM, the pillow is placed on the back

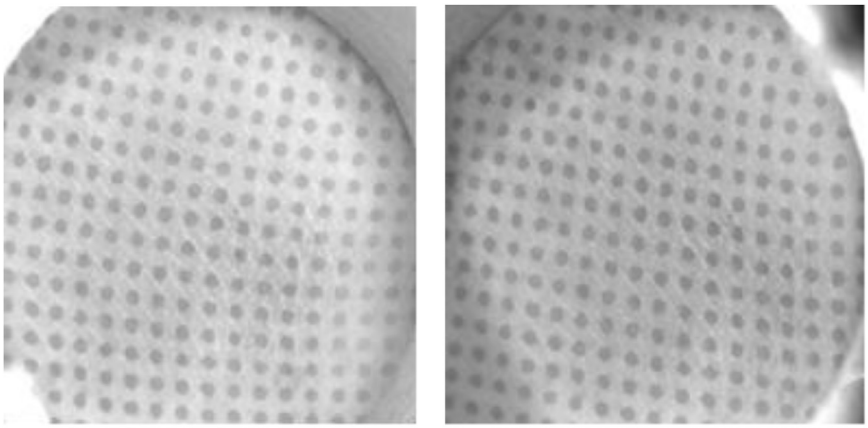

Fig. 3. Pulse images of a certain moment.

of the wrist to keep the wrist steady and comfortable during the whole process of detection. The air supply module consists of an airway and an air pump, and is used to provide a suitable air pressure for the probe.

We first use the air pump to inflate the probe through the airway, then press the airbag probe on the radial artery of the wrist. In this way, pulse beating of the radial artery is transformed into the deformation of thin film. The changes in thin film are contained in the pulse image sequences synchronously captured by two cameras, so the pulse information can be extracted from pulse images.

2.1.3. System software

This includes the following four modules. One is synchronous trigger signal generation software [18], which is used to generate two synchronous signals to trigger the simultaneous exposure of two cameras. The second is dual-camera synchronous acquisition software [18]. It can actualize stable synchronous acquisition of two cameras and automatic continuous image saving. Another is dual-camera stereo calibration algorithm [21], which is used to obtain the calibration parameters of the binocular vision system. The last module is pulse wave extraction and 3D pulse shape reconstruction algorithm, in which methods of image processing and analysis as well as stereo vision theory are adopted to acquire pulse wave and pulse shape.

2.1.4. System working process

The working process of the system, shown as Fig. 2(c), is described as follows. First the system power is turned on, and then the synchronous trigger signal generation software and dual-camera synchronous acquisition software are opened, followed by adjusting the dual-camera fields of view and working distance suitable to the collection of pulse images of wrist radial artery. This all helps collect the clearest images. Then multi-set calibration images are synchronously collected to calibrate the binocular vision system based on the dual-camera stereo calibration algorithm. And then the air pump is adjusted to make probe pressure an appropriate value. The pulse images are continuously collected over a period of time. According to the pulse images, pulse waves and 3D pulse shape can be achieved by pulse wave extraction and 3D pulse shape reconstruction algorithm.

2.2. Pulse wave extraction and 3D pulse shape reconstruction

In the experiment, 10 healthy graduate students were taken as subjects (6 male and 4 female). The pulse images of each subject were continuously collected at the frame rate of 14 frames per second for one minute. See Supplementary Material 1(a) and 1(b) for parts of pulse image sequences of a subject. The subject's pulse images of a particular moment are shown in Fig. 3. The black spots in the images are the mark patterns printed on the thin film, which are used to artificially generate the feature points. According to the repeatability, uniqueness and stability of the feature point, the centroid of each black spot is chosen as the feature point of pulse image. Take a subject's pulse image sequences of 6.5 seconds for example (See Supplementary Material 1(a) and 1(b)), the following describes the detailed process of multipoint pulse wave extraction and dynamic 3D pulse shape reconstruction based on pulse image sequences. Feature point extraction is carried out first, then stereo matching, followed by multipoint spatial coordinate calculation, and finally extraction of pulse wave and 3D reconstruction of pulse shape are realized.

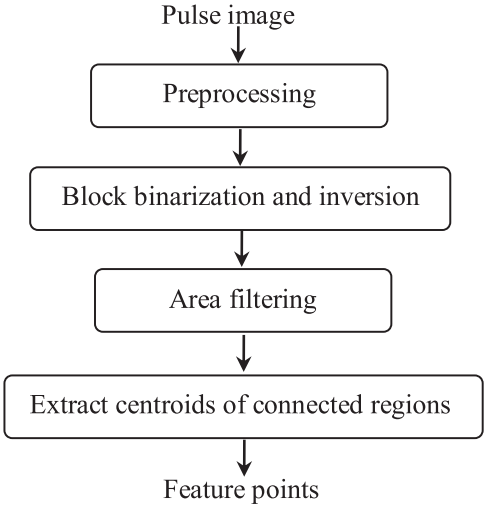

Fig. 4. The process of feature point extraction.

2.2.1. Feature point extraction

Feature point extraction is the key of multipoint pulse wave extraction and dynamic 3D pulse shape reconstruction algorithm. Fig. 4 shows the extraction process. First, pulse images are preprocessed by median filtering. Then block binarization and inversion are implemented. After area filtering, centroids extraction of con-

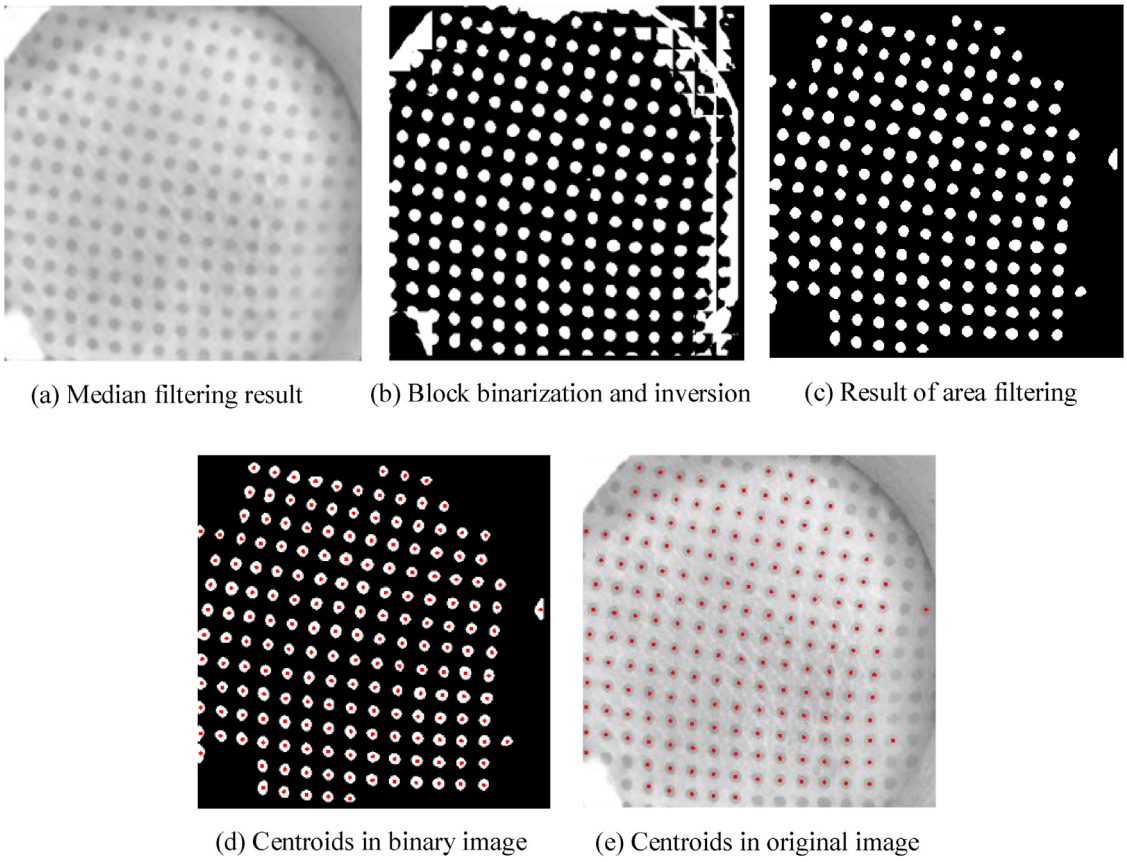

Fig. 5. Process of feature point extraction (shows the processed results of left image). (For interpretation of the references to color in this figure legend, the reader is referred to the web version of this article.)

nected regions are carried out and feature points are finally obtained.

Due to the structures of probe and light source, as well as the angle of camera, the brightness of pulse image is not uniform. In addition, the thin film of the probe is translucent because of its material and thickness, resulting in the skin texture of wrist being reflected in the pulse image through the thin film, as shown in Fig. 3. The existence of these interferences will affect the accuracy of subsequent feature point extraction, and need to be processed. For the superiority of median filtering in noise removal and edge and details information preservation [22], we used the median filter with window size of 7×7 pixels to filter the pulse images. Fig. 5(a) shows the filtered result of the left image in Fig. 3 (only the processed results of left image are shown in this section). The median filter effectively reduces the interferences due to uneven illumination and skin texture.

If each black spot is regarded as a connected region, extracting its centroid as the desired feature point will become very simple. For this reason, the image must be binarized and inversed, and the black spot area is processed into a white connected area, which is easier for programming to extract the centroid. As the image brightness is not uniform, if we use a global threshold for binarization, the result will be poor. Therefore the idea of block binarization is introduced to solve the problem. The image is divided into several blocks, each of which is binarized using its optimum threshold. The number of blocks can be determined according to the specific image. For the pulse images collected in this experiment, each image is divided into 16×16 blocks, each block using Otsu algorithm [23] for binarization. The result of binarization and inversion is shown in Fig. 5(b).

The feature points we expect are the centroids of each black pattern region in the original image. In Fig. 5(b), there are some isolated points, burrs, smaller and larger connected regions. If we directly extract the centroids, we will get some undesirable feature points. Isolated points and burrs can be removed by median filtering. Smaller and larger connected regions appear around the image boundary, usually due to uneven illumination during image acquisition. Feature points of these regions with poor quality will not be used in the following processing. Therefore, before extracting centroids, too small or too large connected regions should be removed by area filtering to ensure the validity and accuracy of the feature points. The result is shown in Fig. 5(c).

The centroid of each connected region is then extracted using Eq. (1) [24]. Where $I(i, j)$ is the gray value of point (i, j) in a connected region S_k, and (X_k, Y_k) are the centroid coordinates of the target region. The red dots in Fig. 5(d) indicate the positions of centroids in binary images, and Fig. 5(e) shows the centroids marked in original images (the marked centroids are magnified to facilitate observation).

$$\begin{cases} X_k = \dfrac{\sum\limits_{(i,j)\in S_k} iI(i,j)}{\sum\limits_{(i,j)\in S_k} I(i,j)} \\ Y_k = \dfrac{\sum\limits_{(i,j)\in S_k} jI(i,j)}{\sum\limits_{(i,j)\in S_k} I(i,j)} \end{cases} \tag{1}$$

2.2.2. Stereo matching

Stereo matching is a necessary procedure to obtain the spatial coordinates of feature points, here it refers to identifying the

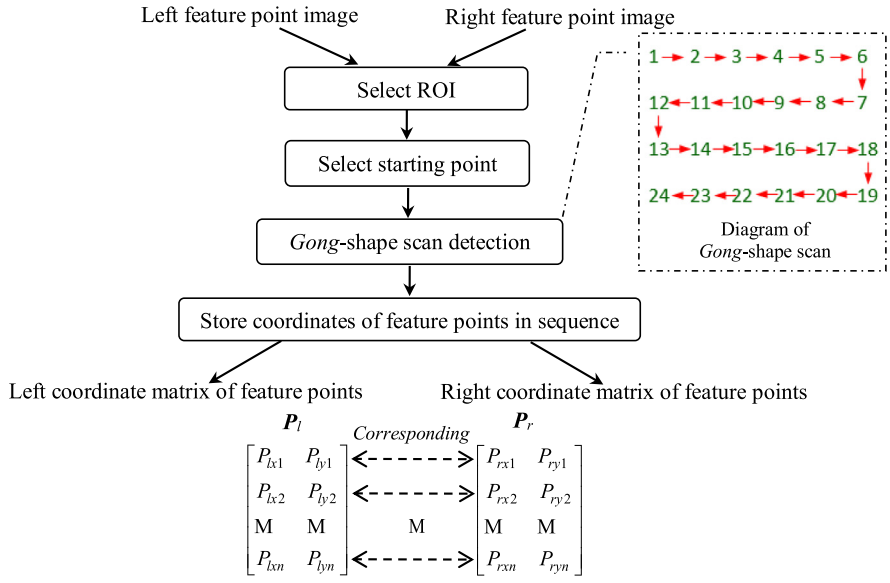

(a) The process of stereo matching

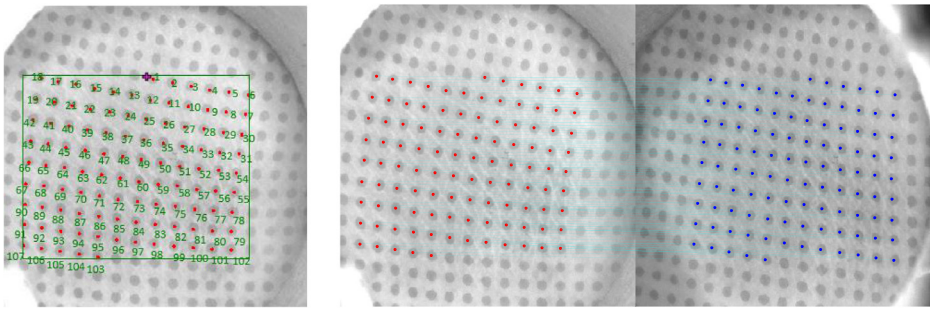

(b) Feature points labeling in ROI (c) Matching result of feature points in the left and right images

Fig. 6. Stereo matching.

one-to-one correspondence relationship between feature points in the left and right images collected at the same time. The process of stereo matching algorithm designed in this paper is shown in Fig. 6(a), which can be described as follows. We first select the region of interest (ROI) that contains conspicuous pulse pulsation, then choose a starting point to detect feature points and carry out sequence labeling using *Gong*-shape scan detection method, and finally store coordinates of feature points in sequence. By performing the above process to the left and right feature point images, we can obtain the left and right coordinate matrices of feature points, and stereo matching is achieved.

From the acquired dynamic pulse image sequences (see Supplementary Material 1(a) and 1(b)), it is observed that the area with conspicuous pulse pulsation is concentrated in the middle of the image, and pulsation is hardly observed in the surrounding area. Moreover, the image quality of the surrounding area is so poor that it is worth no effort to study. The feature points of this region were not extracted in Section 2.2.1. Therefore, the middle region, which has better quality, can be selected as the ROI. It can be seen from Fig. 5(e) that some noise points in the image make it easy for the naked eye to observe the corresponding relation between the left and right feature points, but it is hard for a computer to recognize the relationship. In order to reduce the time spent on the matching process, we select the ROIs which contain the same feature points in the left and right images collected at the same time. That can be achieved by human-computer interaction in Matlab program (i.e., using mouse to click the upper-left and the bottom-right of an image to select the ROI). As shown in Fig. 6(b), the area surrounded by four lines is the ROI, where the pulsation is conspicuous.

If the coordinates of feature point positions in the left and right ROIs are stored in the same order, the matching of the left and right feature points is achieved. In this paper, we first choose a pair of corresponding feature points in the left and right ROIs (usually the first point in the sequencing, such as the feature point "1"in Fig. 6(b)). In the upper-left near this feature point, we manually select a starting point ($P_0(X_0, Y_0)$, the "+" marked point shown in Fig. 6(b)), and then according to the distribution characteristics of feature points in the image, the idea of *Gong*-shape (弓) scan (shown in Fig. 6(a)) is introduced to detect feature points and carry out sequence labeling. The detection idea can be described as follows.

Assuming that the total number of feature points in ROI is n. The distance $D(P_i, P_j)$ between two feature points, P_i *and* P_j, is measured by Euclidean distance, shown as Eq. (2).

$$D(P_i, P_j) = \sqrt{\left(X_i - X_j\right)^2 + \left(Y_i - Y_j\right)^2} \tag{2}$$

***Step* 1**: If$D(P_k,P_0) = \min\{D(P_i,P_0), i = 1, 2, ..., n\}$, then $k = 1$. Namely that the feature point closest to the starting point $(P_0(X_0, Y_0)$ is point number "1", that is P_1;

***Step* 2**: If$|\min_2\{D(P_i,P_k)\} - \min\{D(P_i,P_k)\}| > T$, $i = k+1$, ..., n ($\min_2\{D(P_i,P_k)\}$ means the second smallest value of $\{D(P_i,P_k)\}$, and T is a user-defined threshold), the feature point with $\min\{D(P_i,P_k)\}$ is selected as the point next to

Table 1
Calibration results.

Parameters	Values
$\boldsymbol{F}=[f_l\ f_r]$	[2282.82565 2281.81172]
$\boldsymbol{T}=[t_x\ t_y\ t_z]$	[−44.71803 −0.18991 11.17504]
$\boldsymbol{R}=[r_1\ r_2\ r_3;\ r_4\ r_5\ r_6;\ r_7\ r_8\ r_9]$	[0.8214 −0.0035 0.5703; 0.0002 1.0000 0.0058; 0.5703 −0.0047 0.8214]

$P_k(X_k,Y_k)$; otherwise, the feature point with $\min\{Y_i\}$ is selected; and then $k=k+1$;

***Step* 3**: If $k=n$, end; otherwise, go back to ***Step* 2**.

* *Note that labeled points are no longer included in the next detection range.*

Sequentially store the coordinates of feature points in a matrix. Once the coordinate matrices of the left and right feature points, $\boldsymbol{P}_l$ and $\boldsymbol{P}_y$, are obtained, the stereo matching is completed (shown in Fig. 6(a)). The elements of the corresponding positions in the left and right matrices represent the coordinates of feature points in the left and right images. In the subsequent calculation of feature point spatial coordinates, we can directly access the corresponding coordinates in the left and right images. Fig. 6(b) shows the results of the *Gong*-shape scan, in which the Arabic numerals are the labels of feature points. The selected ROI contains 107 feature points. Fig. 6(c) shows the matching results. It is clear that all feature points are matched correctly.

It is well known that the pulse amplitude is very small, so the frame-to-frame differences of pulse image sequence are extremely small. When the whole image sequence is processed, the human-computer interaction is only carried out when the first frame image is processed, that is, the ROI and the starting point are selected manually in the first frame image. When processing the subsequent frames, it is very efficient to use the ROI and the starting point coordinates selected in first frame instead of manually operating on each frame image.

2.2.3. Multipoint spatial coordinate calculation

Based on the binocular stereo vision theory and the results of system calibration, the 3D spatial coordinates (x, y, z) of each feature point can be obtained precisely according to the mathematical Eq. (3) [19], in which (X_l, Y_l) and (X_r, Y_r) are the coordinates of feature points in the left and right images respectively, and the remaining quantities are the calibration parameters. In this experiment, 29 sets of calibration images with different angles and different positions were collected (as shown in Supplementary Material 2(a) and 2(b)), to calibrate the binocular vision system by the calibration scheme presented in [21], and the results are shown in Table 1. Where $\boldsymbol{F}$ is the effective focal length, $\boldsymbol{T}$ is the translation vector, and $\boldsymbol{R}$ is the rotation matrix. The calculated results are displayed in a 3D coordinate system, as shown in Fig. 7, and the spatial distribution of all feature points is observed.

$$\begin{cases} x = zX_l/f_l \\ y = zY_l/f_l \\ z = f_l(f_r t_x - X_r t_z)/[X_r(r_7X_l + r_8Y_l + f_l r_9) - f_r(r_1X_l + r_2Y_l + f_l r_3)] \end{cases} \tag{3}$$

2.2.4. Extraction of pulse wave

The pulse amplitude information of a certain feature point is contained in the z value of its spatial coordinates. For this feature point, calculating the spatial coordinates at each time point (that is, the time represented by each frame image), finding a suitable reference origin, taking a further step to extract information from z value, we can get the pulse amplitudes of this point at any time. Combining the calculated pulse amplitudes to a data sequence using the same time sequence as used in the pulse image collection process, the pulse wave of the studied feature point can be achieved. In this way, the pulse waves of all feature points can be obtained.

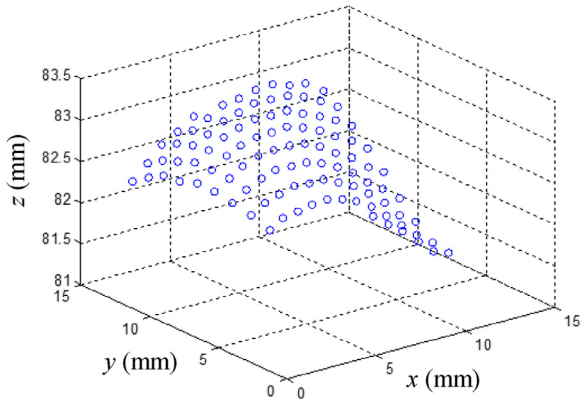

Fig. 7. The spatial distribution of feature points.

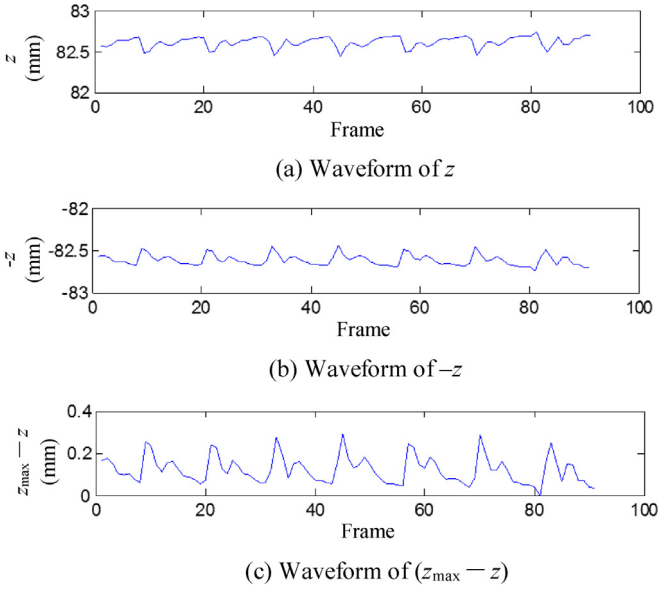

(a) Waveform of z

(b) Waveform of $-z$

(c) Waveform of $(z_{\max} - z)$

Fig. 8. Pulse waves.

The obtained spatial coordinates of feature points are the results of taking the left lens optical center as the origin. According to the binocular pulse detection system shown in Fig. 2(a), when the amplitude of pulse beat is the largest, the probe thin film is closest to the camera, and the z value is the smallest. On the other hand, when the pulse amplitude is the smallest, the probe thin film is furthest away from the camera, and the z value is the largest. Taking the feature point 92 in Fig. 6(b) as an example, the waveform obtained by directly taking the z-value as amplitude is shown in Fig. 8(a). From the waveform characteristics, it looks like the inversion of a pulse wave. So we negate the z-value, that is $-z$, and the resulting waveform is shown in Fig. 8(b). The waveform characteristics reflect the pulse beating trend, but the amplitude values are not obvious. Therefore, it is necessary to change

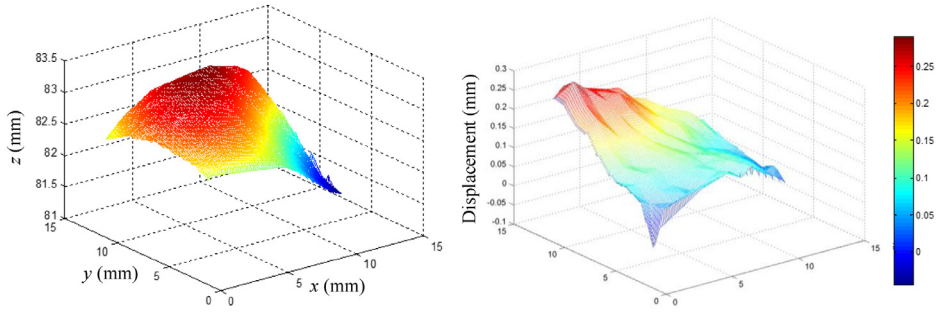

(a) 3D shape of thin film (b) 3D pulse shape

Fig. 9. 3D shape at a moment.

the reference origin to obtain the correct pulse amplitudes. Here, the maximum z-value of the feature point at all times (the entire pulse image sequence) works as a reference value, and the current z-value is subtracted from the maximum z-value to obtain the current pulse amplitude, as shown in Eq. (4). That is, convert the reference origin from the left lens optical center to the trough point of the pulse wave to achieve the waveform as shown in Fig. 8(c), in which the waveform periodicity is clear, the main wave and dicrotic wave are obvious, and much in line with the characteristics of the pulse wave.

$$\text{Amplitude} = z_{\max} - z \tag{4}$$

2.2.5. 3D reconstruction of pulse shape

The 3D pulse shape can be reconstructed by using the following approach. We first reconstruct the 3D shape of thin film at any time, then find the appropriate reference time to obtain the 3D pulse shape.

Fig. 7 is only a preliminary observation of spatial distribution of a limited number of feature points. To achieve a complete 3D shape of thin film in the ROI at a given time, the number of feature points should be as many as possible in this region. However, the number of mark patterns printed on the probe's thin film with extremely small area is limited, so we use the interpolation method to solve this problem. Based on the spatial coordinates of feature points, the linear interpolation method is used to obtain a 3D image. Fig. 9(a) is the results of interpolation based on Fig. 7, vividly presenting the 3D thin film shape of the ROI.

When the longitudinal displacements of all points on the thin film reaches the minimum, the deformation of the thin film is the smallest. At this moment, the dilation of radial artery is minimal, and is closest to the natural state of the radial artery. Take the 3D shape of the thin film at this moment as a reference value, and calculate the difference between 3D shape of the thin film at another moment and this reference value, then we can obtain the relative displacement of skin surface caused by the pulse beating. We call this the 3D pulse shape. Fig. 9(b) is the 3D pulse shape of a moment. At this moment, the points with larger displacements are located at the positions with more conspicuous pulsations.

3. Results

3.1. Pulse amplitude

Fig. 10 shows the statistical results of the maximum pulse amplitudes sorting for all feature points. As we can see, among all the feature points studied, feature point 6 has the smallest pulsation range with maximum amplitude 0.0519 mm, and feature point 92 has the largest pulsation range with maximum amplitude 0.2919 mm. It can be seen from Fig. 6(b) and Supplementary Material 1(a) and 1(b) that feature point 92 is close to the center of the vessel but point 6 is located away from the center of the vessel. The result given in Fig. 10 corresponds to the characteristics of pulse amplitude that it decreases as the distance from the artery center increases.

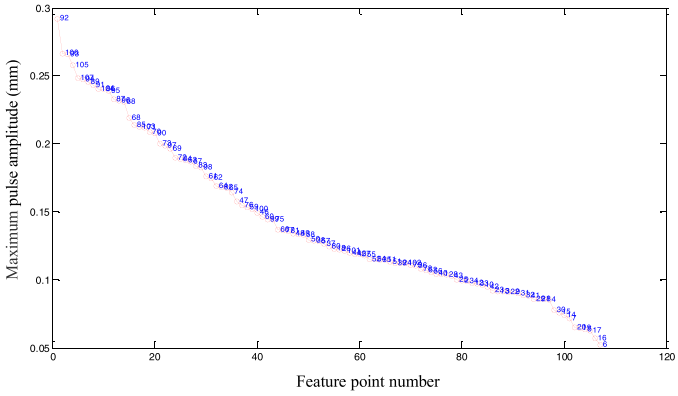

Fig. 10. Sorting of maximum pulse amplitudes of all feature points.

Fig. 11(a) shows the waveforms of seven consecutive feature points along the direction close to the vessel axis. As can be seen from the waveforms, the differences of pulse amplitudes of feature points in this direction are not obvious. Fig. 11(b) shows the waveforms of seven consecutive points along the direction close to the cross-section of the vessel. As is shown in the figure, the closer to the vessel center, the larger the pulse amplitude is, and the farther from the vessel center, the smaller the pulse amplitude is. The above results are in accordance with the characteristics of pulse wave.

3.2. Pulse rate

In order to further verify the effectiveness of the proposed method, the extracted waveforms are further processed and the pulse rate is extracted for analysis. Taking the waveform of feature point 92 as an example, using the peak extraction method introduced in [25], we can get the positions of seven peak points in 91 frames. As shown in Fig. 12, the red circles mark the peak points and the red Arabic numerals are the occurrence time of peak points, i.e., the frame numbers. The period of pulse signal can be obtained from the positions where the peak points are located. The difference between the positions of each two adjacent peak

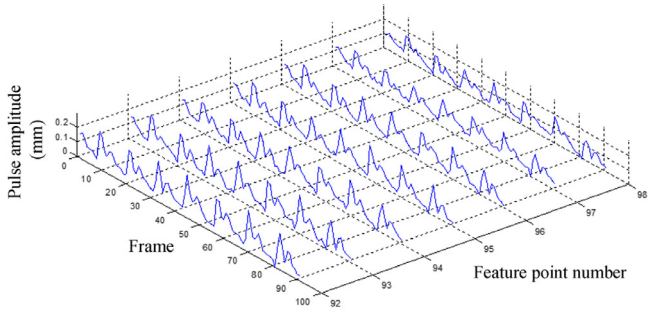

(a) Waveforms of 7 consecutive feature points along the direction close to the vessel axis

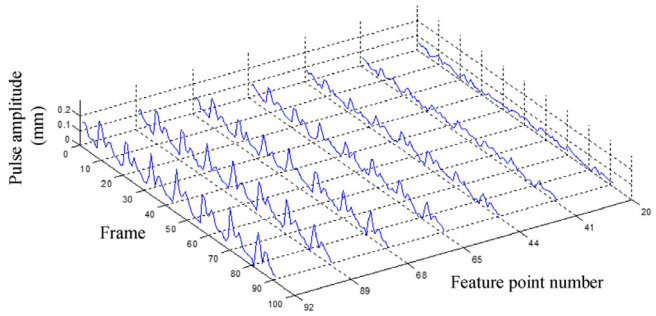

(b) Waveforms of 7 consecutive feature points along the direction close to the cross-section of the vessel

Fig. 11. Pulse waveforms in two directions.

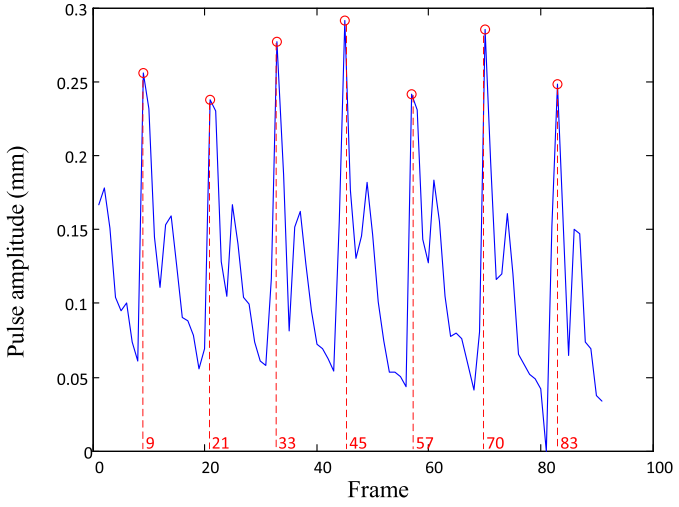

Fig. 12. Detection result of peak points. (For interpretation of the references to color in this figure legend, the reader is referred to the web version of this article.)

points can reflect the period. In order to obtain an accurate period, the data should be fully utilized to calculate average period T by Eq. (5). Where L is the array composed of the red Arabic numerals in Fig. 12, *diff* (L) is the difference between the elements of L, *sum* represents summing, *length* is the length of the array, and 14 refers to the camera frame rate when capturing images (unit: frames per second). After obtaining T, according to formula (6), we can easily get the pulse rate f of this pulse signal, which is 68.1081 times/min. The obtained pulse rate is in the range of 60–100 times/min of normal adult pulse rate.

$$T = (sum(diff(L))/length(diff(L)))/14 \tag{5}$$

$$f = (1/T) \times 60 \tag{6}$$

3.3. Pulse shape

Adopting the proposed method presented in Section 2.2.5, the 3D reconstruction of the thin film shape and pulse shape are achieved according to the pulse image sequence. Fig. 13 shows 3D shapes of the thin film at six different moments. Fig. 14 shows 3D pulse shapes of the same six moments. According to Fig. 13, we can hardly see the difference in the shapes of thin film between different moments. However, the relative displacements of the thin film caused by pulse beating can be seen clearly in Fig. 14.

From frame 44 to frame 49, the change trend of relative displacements is "upward → downward → downward → upward → upward", which is the same as the change trend of pulse waveform of feature point 92 shown in Fig. 15. Fig. 16 shows the position corresponding relations between feature points distributed in image plane and their displacements displayed in 3D space (take frame 45 for example). Since feature point 92 is close to the center of the vessel, its surrounding area has the most obvious deformation, and the feature points in this area have maximum longitudinal displacements. On the contrary, because feature point 6 is far away from the center of the vessel, so the deformation of its surrounding area is not obvious, and the feature points in this area have small longitudinal displacements. This result is consistent with the statistical result shown in Fig. 10. The correctness of change trend and position correspondence, and the similarity between the reconstructed pulse shape and result in [26], indicate that our method is effective and the pulse shape is correct.

Composing the reconstructed 3D pulse shape images to a new image sequence, and using the same time sequence and frame rate as used in the image collection process, we can make a video of dynamic 3D pulse shape by linking all the frames of 3D image together, which makes the pulse beats more intuitively presented. The result is shown in Supplementary Material 3. The dynamic 3D shape of the thin film can be acquired using the same method, and is presented as Supplementary Material 4, which shows the movement of the thin film. Similarly, a dynamic 3D view of a single feature point can be obtained to facilitate observation of single-point beating, as shown in Supplementary Material 5.

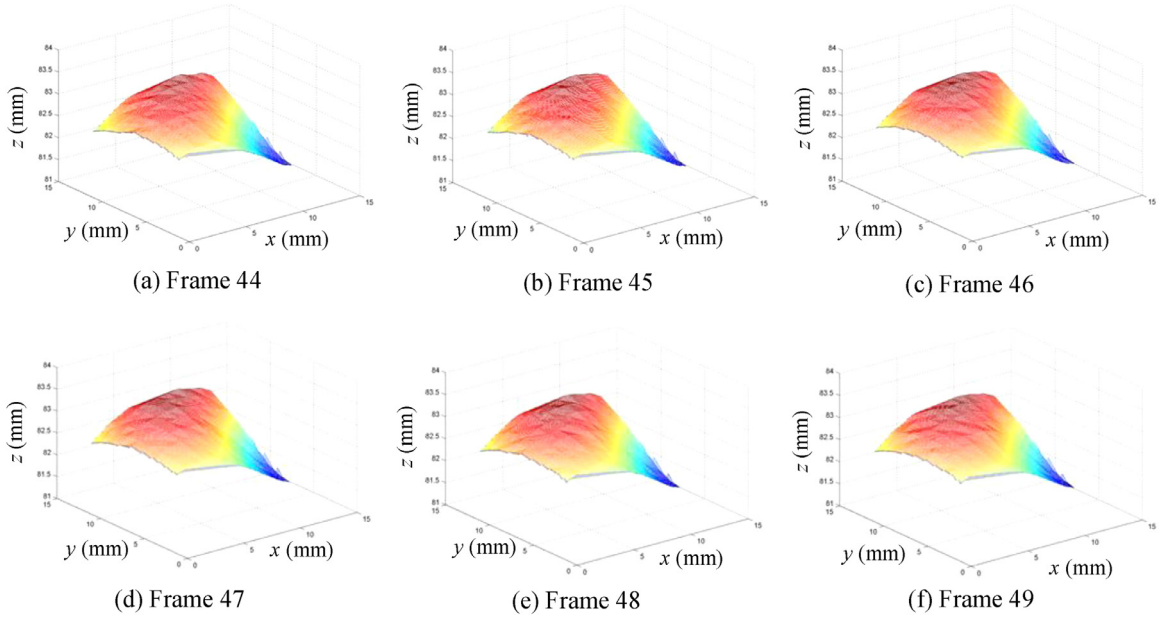

Fig. 13. Thin film shapes at different moments.

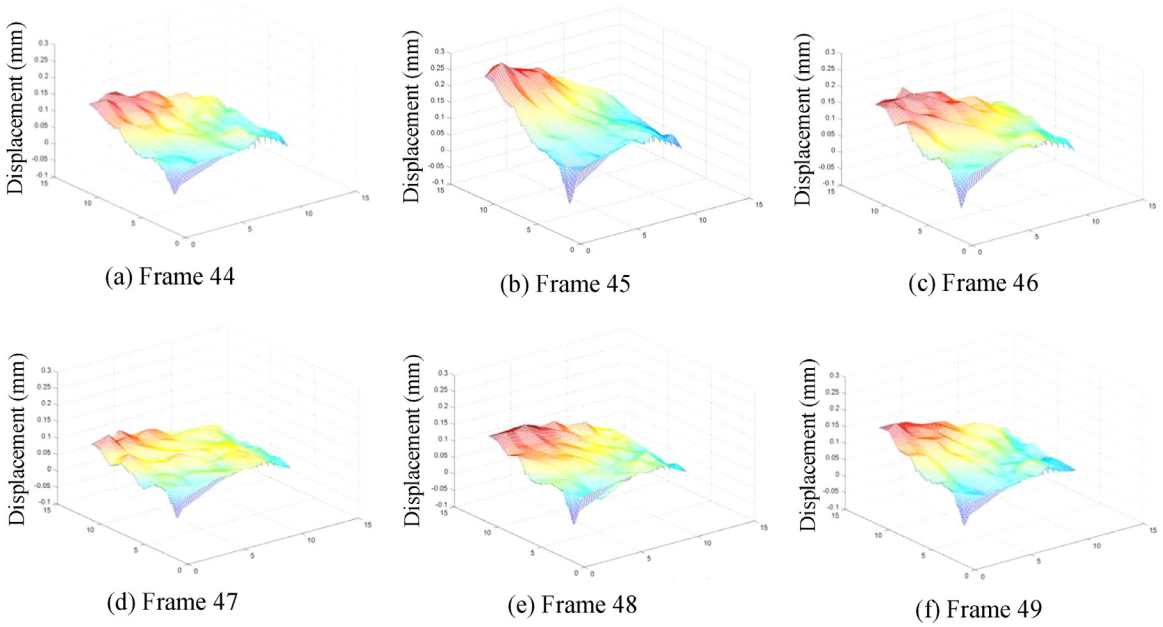

Fig. 14. Pulse shapes at different moments.

4. Discussion

In this section, the proposed method is compared with other methods, and the limitation as well as the future work are discussed.

4.1. Comparison with other methods

Many approaches to pulse detection of the radial artery have been proposed in recent years. Mainly advances are state-of-the-art wearable tactile sensors, but most commonly referred to as strain and pressure sensors [27–30]. These sensors transform the pulse beats into weak voltage or current outputs, not the exact values of displacement. T. Sirkis designed a new fiber sensor for non-contact estimation of vital bio-signs, which was incorporated into a shirt to produce smart clothing, but the measured wrist pulse waves are not very good judged from the results presented in [31]. Y.F. Chung's research group obtained 3D pulse mapping based on pulse sensor array, but the measured amplitudes were not the exact displacement values [26,32,33]. Some pulse information detection methods based on imaging technology were also studied, such as infrared imaging [34], Optical Coherence Tomography [35], and ultrasound imaging [36], but no exact displacement values of pulse were obtained by these methods.

The method presented in this paper is compared with the following two methods in order to further verify the correctness of the pulse rate. One is the method based on image entropy I proposed in [17], and the other is the method based on pattern area variation previously proposed by our research group [37]. The synchronism of the pulse waveforms obtained by the three methods,

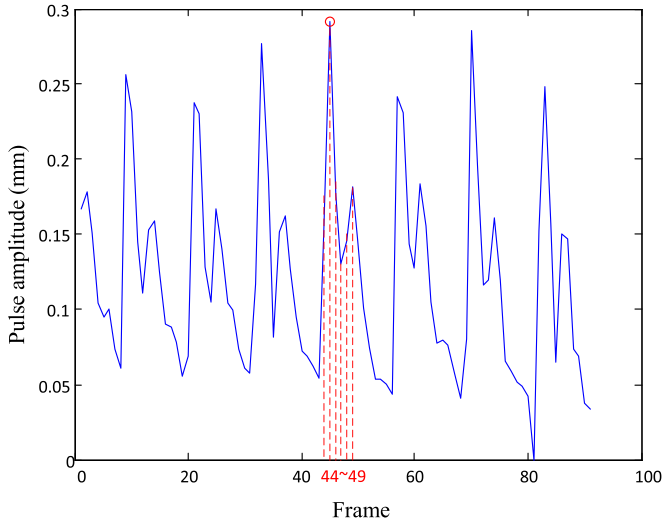

Fig. 15. Annotation of frame 44 to frame 49 on the pulse waveform.

shown in Fig. 17, is analyzed. Fig. 17(a) is the waveform of feature point 92 obtained by the method presented in this paper, Fig. 17(b) shows the waveform of the right image sequence based on image entropy method, and Fig. 17(c) is the waveform of feature point 92 in the left image sequence obtained by the method based on the area variation of pattern printed on the probe thin film. It can be seen that the peak points of the three waveforms appear simultaneously, that is the waveforms achieved by the three methods are synchronous, which indicates that the obtained pulse rates are the same. Thus the correctness of pulse rate extracted by the method proposed in this paper is verified. In addition, the method of [17] can only get the trend of pulse of the radial artery, but not the true pulse amplitude value. Moreover, it can be seen from Fig. 17 that amplitude values obtained by the proposed method are greater than those of [37], and the waveform is better. Therefore, the proposed method is more accurate than the other two previously used methods, and it is an effective pulse detection method.

4.2. Limitation of the proposed method and future work

According to Three Positions and Nine Indicators, the pulse feeling method can be divided into Simultaneously Palpation (SP) and the Pressing with One Finger (PWOF) in TCM [26]. The proposed binocular pulse detection system can only simulate PWOF. The pulses from Cun, Guan and Chi three positions should be collected as a whole for accurate pulse diagnosis. So the designed system needs to be improved to a three-probe detection system in future study.

More studies are needed to further improve the proposed system. For example, a mechanical device for wrist and finger fixation will be helpful in keeping the hand fixed during the whole detection process, and improve the accuracy of detection results. A reasonable verification scheme could be designed to further verify the accuracy of extracted pulse waveform and reconstructed 3D pulse shape. Upgrading the synchronous acquisition program and related hardware can achieve a higher camera frame rate of synchronous acquisition and improve the accuracy of the result. Improving system function, realizing the automatic control and synchronous acquisition of pulse feeling pressure and probe internal pressure can benefit objective and necessary multi-source analysis data for the follow-up continuous blood pressure wave extraction. It is neces-

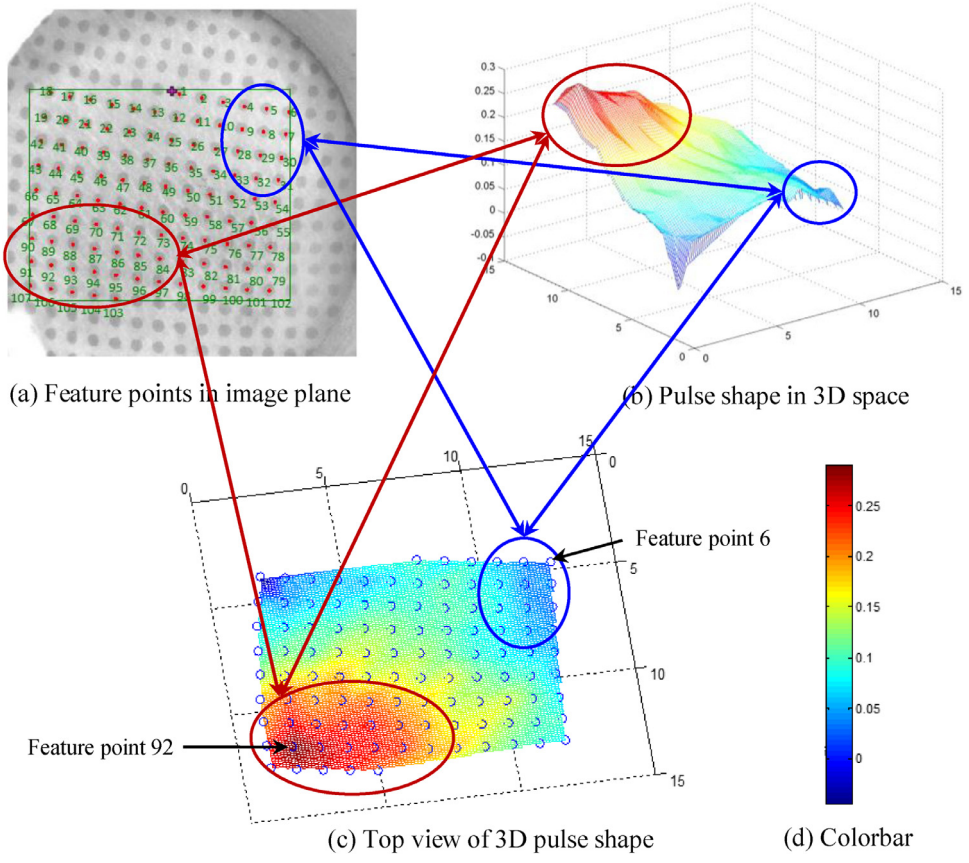

Fig. 16. The position corresponding relations between feature points distributed in image plane and their displacements displayed in 3D space.

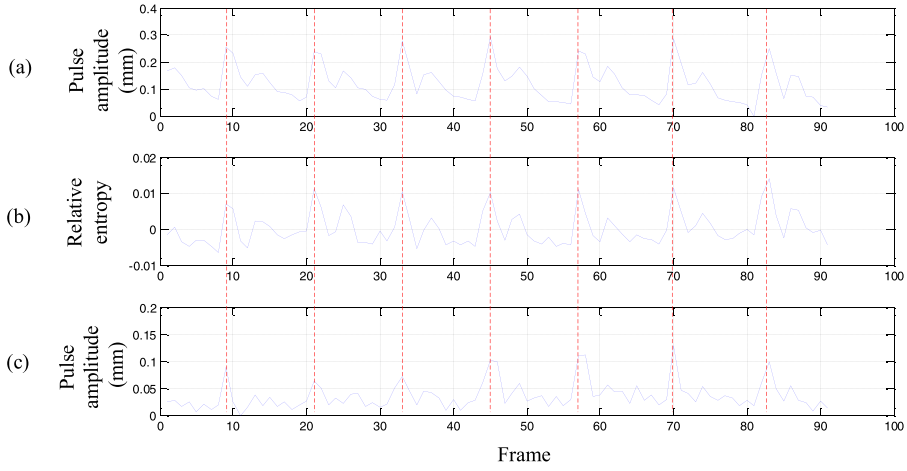

Fig. 17. Pulse waves obtained by three different methods. (a) Method proposed in this paper; (b) Method based on image entropy [17]; (c) Method based on pattern area variation [37].

sary to find smaller cameras to replace the large industrial cameras used in the system. It is also very important to propose a suitable automatic calibration algorithm for this system. All of the above work is for the purpose of making the designed system intelligent, light and portable, simple and easy to apply.

Furthermore, after the improvements, the system has the potential to make pulse diagnosis more objective, and even realize automatic pulse diagnosis. This is the ultimate goal of our research on this system.

5. Conclusions

Based on the theory of binocular vision measurement, the binocular pulse detection system was designed. In the proposed method, the centroid of mark pattern was taken as the feature point. Combined with digital image processing method, the pulse image sequences acquired by the system were analyzed. Finally, the extraction of multipoint pulse waves and the dynamic 3D reconstruction of pulse shape were realized. The experimental results, analyses of pulse amplitude, pulse rate, and pulse shape, comparison with other methods all show that the proposed method is effective for pulse information detection. In addition, since the proposed image-based method can detect full information of pulse of the radial artery, more information about physiological parameters such as systolic duration and diastolic duration can be obtained based on the time-domain analysis of pulse wave. Pulse width and pulse length can also be obtained in time-spatial domain.

Overall, the binocular pulse detection system designed in this study has high application value and broad application prospects, and could contribute to the further development of objective and automatic pulse diagnosis.

Conflict of interest

We declare that there is no conflict of interest related to this paper.

Acknowledgments

This work was supported by the National Natural Science Foundation of China (No. 81360229, titled “Artery blood pressure waveform measurement based on the deformation visualization in time-spatial domain of airbag”). The authors would like to thank Beijing Sanbao Xingye Vision Technology Company Limited for their continuous support.

Supplementary materials

Supplementary material associated with this article can be found, in the online version, at doi:10.1016/j.cmpb.2017.11.025.

References

[1] J.N. Lygouras, P.G. Tsalides, Optical-fiber finger photo-plethysmograph using digital techniques, IEEE Sens. J. 2 (1) (2002) 20–25, doi:10.1109/7361.987057.
[2] Y.Z. Yoon, M.H. Lee, K.S. Soh, Pulse type classification by varying contact pressure, IEEE Eng. Med. Biol. 19 (6) (2000) 106–110, doi:10.1109/51.887253.
[3] Y. Lin, H. Leng, G. Yang, H. Cai, An intelligent noninvasive sensor for driver pulse wave measurement, IEEE Sens. J. 7 (5) (2007) 790–799, doi:10.1109/JSEN.2007.894923.
[4] A.B. Joshi, A.E. Kalange, D. Bodas, S.A. Gangal, Simulations of piezoelectric pressure sensor for radial artery pulse measurement, Mater. Sci. Eng. B. 168 (1-3) (2010) 250–253, doi:10.1016/j.mseb.2010.01.012.
[5] Z.G. Zhang, X. Niu, D.Z. Chen, H. Sha, Study on the relations between three--dimensional motion of radial artery and pulse force, in: Proceedings of 2006 International Forum on Innovation and Development Situation of Traditional Medicine, 2006, pp. 150–153.
[6] Z.G. Zhang, X. Niu, X.Z. Yang, Relationship between radial cyclic kinetic energy of radial artery and pulse force, J. B. Univ. Tradit. Chin. Med. 30 (12) (2007) 813–815, doi:10.3321/j.issn:1006-2157.2007.12.007.
[7] G.C. Jin, M. Yu, Research of multi-point pulse wave computer measurement system using PVDF, J. Tsinghua Univ. 39 (8) (1999) 117–120, doi:10.3321/j.issn:1000-0054.1999.08.030.
[8] W.C. Tang, C.Y. Liu, Y.P. Zhao, Research on the Cun-Guan-Chi pulse detecting system, Chin. J. Med. Inst. 29 (3) (2005) 164–166, doi:10.3969/j.issn.1671-7104.2005.03.003.
[9] J.H. Wu, R.S. Chang, J.A. Jiang, A novel pulse measurement system by using laser triangulation and a CMOS image sensor, Sensors 7 (12) (2007) 3366–3385 PMCID: PMC3841900.
[10] K. Malinauskas, P. Palevicius, M. Ragulskis, V. Ostasevicius, R. Dauksevicius, Validation of noninvasive MOEMS-assisted measurement system based on CCD sensor for radial pulse analysis, Sensors 13 (4) (2013) 5368–5380, doi:10.3390/s130405368.
[11] Y.F. Chung, C.S. Hu, Y.W. Chu, C.H. Luo, Exploring the conventional pulse conditions using bi-sensing pulse diagnosis instrument, in: 2011 4th International Conference on Biomedical Engineering and Informatics (BMEI), 2011, pp. 744–748, doi:10.1109/BMEI.2011.6098473.
[12] C.H. Luo, Y.F. Chung, C.S. Hu, C.C. Yeh, X.C. Si, D.H. Feng, Y.C. Lee, S.I. Huang, S.M. Yeh, C.H. Liang, Possibility of quantifying TCM finger-reading sensations: I. Bi-sensing pulse diagnosis instrument, Eur. J. Integr. Med. 4 (3) (2012) 255–262, doi:10.1016/j.eujim.2012.03.003.
[13] Y.F. Chung, Y.W. Chu, C.Y. Chung, C.S. Hu, New vision of the pulse conditions using bi-sensing pulse diagnosis instrument, in: 2013 1st International Conference on Orange Technologies (ICOT), 2013, pp. 5–8, doi:10.1109/ICOT.2013.6521143.
[14] X.W. Wang, Y. Gu, Z.P. Xiong, Z. Cui, T. Zhang, Silk-molded flexible, ultrasensitive, and highly stable electronic skin for monitoring human physiological signals, Adv. Mater. 26 (9) (2014) 1336–1342, doi:10.1002/adma.201304248.
[15] A.H. Zhang, L. Zhu, Sphygmus Dynamic Image Information Collecting System, 2007, Patent number: CN200610042994.9.
[16] A.H. Zhang, L. Zhu, H.Z. Dang, Pulse Dynamic Image Information Detecting Device, 2012, Patent number: CN201010196991.7.

[17] D.M. Lin, A.H. Zhang, F.L. Yang, X.L. Chen, A novel pulse wave extraction algorithm based on image entropy, J. Cent. S. Univ. 44 (9) (2013) 3731–3738 Accession number: 20134917048486.
[18] D.M. Lin, A.H. Zhang, R. Shen, P. Wang, L.M. Yang, X.L. Chen, Dual-camera synchronous acquisition method for binocular vision pulse measurement system, J. Jilin Univ. 45 (6) (2015) 1999–2006, doi:10.13229/j.cnki.jdxbgxb201506038.
[19] G.J. Zhang, Vision Measurement, Science Press, Beijing, 2008.
[20] B.K.P. Horn, Robot Vision, The MIT Press, Cambridge MA, 1986.
[21] D.M. Lin, A.H. Zhang, P. Wang, Y.Q. Ma, L.M. Yang, Z.F. Liu, Application of Zhang's calibration method in binocular vision pulse measurement system, J. Lanzhou Univ. Technol. 42 (2) (2016) 78–85.
[22] R.C. Gonzalez, R.E. Woods, Digital Image Processing, third ed., Publishing House of Electronics Industry, Beijing, 2010.
[23] N. Ohtsu, A threshold selection method from gray-level histograms, IEEE Trans. Syst., Man Cybern. 9 (1) (1979) 62–66, doi:10.1109/TSMC.1979.4310076.
[24] Q.F. Yu, H.W. Lu, X.L. Liu, Precision Measurement and Motion Measurement Based On Image, Science Press, Beijing, 2002.
[25] H.Y. Xing, R.Q. Xu, C.S. Wang, Pulse signal feature research based on empirical mode decomposition, Chin. J. Sci. Inst. 3 (30) (2009) 576–602, doi:10.3321/j.issn:0254-3087.2009.03.028.
[26] Y.F. Chung, C.S. Hu, C.C. Yeh, C.H. Luo, How to standardize the pulse-taking method of traditional Chinese medicine pulse diagnosis, Comput. Biol. Med. 43 (4) (2013) 342–349, doi:10.1016/j.compbiomed.2012.12.010.
[27] T.T. Yang, D. Xie, Z.H. Li, H.W. Zhu, Recent advances in wearable tactile sensors: materials, sensing mechanisms, and device performance, Mater. Sci. Eng. R. 115 (2017) 1–37, doi:10.1016/j.mser.2017.02.001.
[28] J.M. Wu, C.C. Lee, Y.H. Lin, High sensitivity wrist-worn pulse active sensor made from tellurium dioxide microwires, Nano Energy 14 (2015) 102–110, doi:10.1016/j.nanoen.2015.02.009.
[29] A. Bongrain, L. Rousseau, L. Valbin, N. Madaoui, G. Lissorgues, F. Verjus, P. Chapon, A new technology of ultrathin AlN piezoelectric sensor for pulse wave measurement, Proc. Eng. 120 (2015) 459–463, doi:10.1016/j.proeng.2015.08.668.
[30] D.M. Wang, D. Zhang, G.M. Lu, A robust signal preprocessing framework for wrist pulse analysis, Biomed. Signal Process. Control 23 (2016) 62–75, doi:10.1016/j.bspc.2015.08.002.
[31] T. Sirkis, Y. Beiderman, S. Agdarov, Y. Beiderman, Z. Zalevsky, Fiber sensor for non-contact estimation of vital bio-signs, Opt. Commun. 391 (2017) 63–67, doi:10.1016/j.optcom.2017.01.013.
[32] C.H. Luo, C.J. Su, T.Y. Huang, C.Y. Chung, Non-invasive holistic health measurements using pulse diagnosis: I. Validation by three-dimensional pulse mapping, Eur. J. Integr. Med. 8 (2016) 921–925, doi:10.1016/j.eujim.2016.06.017.
[33] Y.W. Chu, C.H. Luo, Y.F. Chung, C.S. Hu, C.C. Yeh, Using an array sensor to determine differences in pulse diagnosis - three positions and nine indicators, Eur. J. Integr. Med. 6 (5) (2014) 516–523, doi:10.1016/j.eujim.2014.04.003.
[34] W.B. Zhou, B. Jing, D. Qu, G.H. Yuan, C.Y. Wang, H.Y. Li, A novel non-contact pulse information detection method based on the infrared sequence images, in: Communication Systems Information Technology, in: LNEE, 100, 2011, pp. 259–265, doi:10.1007/978-3-642-21762-3_33.
[35] Y.H. Shen, Z.F. Li, H. Li, H.Y. Chen, Detection and analysis of multi-dimensional pulse wave based on optical coherence tomography, in: Proceedings of SPIE, 2014 pp. 926826-926826-6, doi:10.1117/12.207167.
[36] R.X. Li, A. Ip, E. Sanz-Miralles, E.E. Konofagou, Noninvasive evaluation of varying pulse pressures invivo using brachial sphymomanometry, applanation tonometry, and pulse wave ultrasound manometry, Artery Res. 18 (2017) 22–28, doi:10.1016/j.artres.2017.02.002.
[37] Y.J. Mao, Study on Relation of Visual Fatigue and Sub-Health Based on Pulse Signals, Lanzhou University of Technology, Lanzhou, 2010, doi:10.7666/d.Y1712503.